Submitted to JCP

Nonresonant ionization of oxygen molecules by femtosecond pulses: plasma dynamics studied by time-resolved terahertz spectroscopy

Zoltan Mics[1], Filip Kadlec[1], Petr Kužel[1*] , Pavel Jungwirth[2], Stephen E. Bradforth[3], and V. Ara Apkarian[4]

[1] *Institute of Physics, Academy of Sciences of the Czech Republic, and Center for Biomolecules and Complex Molecular Systems, Na Slovance 2, 182 21 Prague 8, Czech Republic*

[2] *Institute of Organic Chemistry and Biochemistry, Academy of Sciences of the Czech Republic, Biomolecules and Center for Biomolecules and Complex Molecular Systems, Flemingovo nam. 2, 166 10 Prague 6, Czech Republic*

[3] *Department of Chemistry, University of Southern California, Los Angeles, CA 90089, USA*

[4] *Department of Chemistry, University of California, Irvine, CA 92697, USA.*

*To whom correspondence should be addressed: kuzelp@fzu.cz

Abstract

We show that optical pump-terahertz probe spectroscopy is a direct experimental tool for exploring laser induced ionization and plasma formation in gases. Plasma was produced in gaseous oxygen by focused amplified femtosecond pulses. The ionization mechanisms at 400 nm and 800 nm excitation wavelength differ significantly being primarily of a multiphoton character in the former case and a strong-field process in the latter case. The generation of the plasma in the focal volume of the laser, and its expansion on sub-nanosecond time scale scale is directly monitored through its density dependent susceptibility. A Drude model used to evaluate the plasma densities and electron scattering rates successfully captures the observations for a wide range of pump intensities. In addition, rotational fingerprints of molecular and ionic species were also observed in the spectra.

1 Introduction

The strong fields generated in short-pulse intense laser sources are employed in a large variety of applications. Ionization,[1] supercontinuum generation,[2] the generation of high harmonics,[3] attosecond and X-ray pulses,[4, 5, 6] are notable examples in rarefied gaseous media. In condensed matter, the applications range from ablation,[7, 8] controlled damage,[9, 10] micromachining,[11, 12] to the high energy density physics of fusion.[13] In all these examples, ionization is either a principle step in the processes at issue or an inseparable side effect. Since the photogenerated plasma in the focal volume of a laser is most strongly coupled to the applied radiation, it plays an important role in the propagation of the field[14] and in mediating the field-material interaction.[15] Indeed, the principles of cascade electron impact ionization introduced to describe the first realizations of laser-induced breakdown,[16, 17] are quite generally applicable to condensed media, as has been shown quantitatively in strong-field ionization in simple liquids.[18, 19] Moreover, studies of controlled laser damage in dielectrics clearly illustrate that a significant part of the physics at work is due to laser driven collective excitations of the photogenerated microplasma.[20, 21] For the most part, such conclusions are made indirectly: by observing photodetached electrons or ions in gas phase applications; by ex post analysis of tracks in solids;[21] by noting negative dispersion in self-phase modulation,[19] or spectra shift of the propagated beams that can be ascribed to free carriers.[22, 23, 24] The latter effects are key to the application of plasma waveguides to compress coherent extreme UV and X-ray pulses in the sub-femtosecond regime.[25] Clearly, direct diagnosis of the evolution of plasmas in space and time would greatly aid our understanding of these processes and in advancing their applications. Time resolved terahertz spectroscopy is such a tool. We demonstrate this contention by characterizing the non-resonant, strong-field induced ionization

of gaseous molecular oxygen.

Beside its contribution to laser plasmas generated in air,[26] ionized oxygen, O_2^+, plays an important role in the upper atmosphere, as the main source of $O(^1S)$,[27, 28] , which in turn is responsible for the auroral radiation.[29, 30] The dissociative recombination process which generates $O(^1S)$ from O_2^+ is strongly dependent on the initial vibrational excitation of the parent ion.[31, 32] The internal vibrational distribution of nonresonantly photogenerated O_2^+ is strongly dependent on the intensity of the radiation source, and shows anomalous distributions when generated with ps and fs pulsed radiation.[33, 34] While understanding of the formation dynamics of photogenerated ions in strong fields is valuable, in the present we concentrate on the direct analysis of the non-resonant, strong-field induced formation and decay of the plasma in gas phase O_2.

THz probing of the gas phase has been extensively applied for the detection and characterization of rotating molecules.[35, 36] At the same time, the THz pulses are highly sensitive to the presence of mobile charge carriers in ionized gases. THz time-domain spectroscopy was used to characterize with sub-μs time resolution a He discharge plasma build-up induced by a high voltage bias.[37] These measurements yielded the plasma frequency and the collision rate which were both found in the sub-THz range. The generation of THz pulses by photoionization of air with and without an electrical bias field has also been recently reported.[38, 39, 40].

In this paper we describe multi-photon and strong-field ionization of pure molecular oxygen gas. We have applied a THz probe to the detection of the developing free electron gas generated by focused 400 nm and 800 nm 50 fs pulses and for characterization of neutral and ionic molecular species.

2 Experimental details

The experimental setup was similar to that described in [41] and it is schematically shown in Fig. 1. Briefly, amplified 1 mJ laser pulses with a duration of 55 fs, a mean wavelength of 810 nm, and a repetition rate of 1 kHz were used to ionize O_2 molecules (up to 80% of the laser power) and to generate and detect ultrashort THz pulses (20% of the power). Two ellipsoidal mirrors were used for focusing of the THz beam. A 0.5 mm circular aperture was placed in their common focal point so that about 10% of the THz field amplitude passed through. The whole THz setup was enclosed in an experimental chamber which was evacuated and re-filled with pure oxygen at atmospheric pressure.

To distinguish between different regimes of the photo-ionization process the pump–probe experiments were carried out for two pump wavelengths (the fundamental one at 810 nm and the second harmonic at 405 nm obtained using a 0.35 mm thick LBO crystal) and for two polarization states of the pump beam (linear and circular). Each of these measurements was performed as a function of quasi-continuously varying pump pulse energy. A great care was devoted to precise control of the pump intensity without modification of the pump–probe delay and of other relevant pump pulse characteristics. The schemes we used are summarized in the Appendix A. The pump beam was focused by a $f = 400$ mm lens to the center of the aperture. The width of the excitation beam in the waist was determined by means of a CCD beam profiler at low power as $2w = 0.16$ mm. Throughout this paper we characterize the pump strength by the peak intensity I of the pump pulse expressed in TW/cm^2 and calculated from the average laser power determined by a power meter, from the beam diameter and from the pulse length assuming Gaussian spatial and temporal profile of the pulse. We estimate that the systematic error of the absolute determination of the value $\log I$ can reach ± 0.3; however, random errors

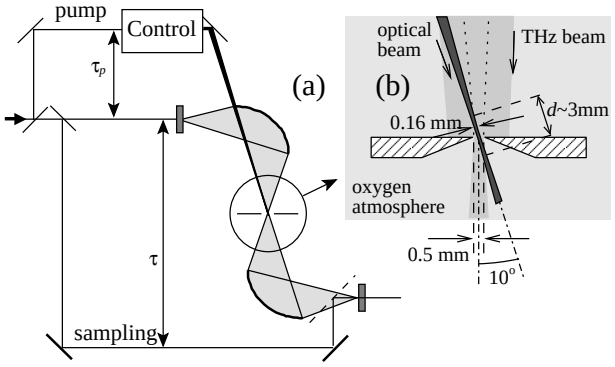

Figure 1: Experimental scheme. The pump beam branch contains a specific arrangement for a careful control of the pump beam attenuation and polarization and a second harmonic stage (see Appendix for further details). Inset: detail of the geometry of the aperture and beams and of the interaction volume.

within a series of measurements do not exceed 10% of I.

In principle, an acquisition of a two dimensional (2D) transient data $\Delta E(\tau, \tau_p)$ — where τ_p is the pump–probe delay and τ is the THz waveform sampling time (see Fig. 1) — provides a full information about the ultrafast dynamics in the far infrared.[42] The measured 2D time-domain data then usually require an appropriate deconvolution yielding the transient THz response function free of artifacts due to the frequency mixing and to the instrumental functions.[43, 44] In the present case, the experimental results indicate that the transient THz signal varies only very slowly with the pump–probe delay: a significant variation starts to show up after a delay of about hundred of picoseconds which largely exceeds the THz pulse length. In this case, it is possible, without loss of information, to obtain THz spectra of the photoexcited state from one dimensional experimental data, i.e., a single THz waveform measured for a given pump–probe delay.

Three kinds of experiments were performed:

1. Measurements of the peak waveform values $\Delta E_{\max}$ (with τ, τ_p fixed) as a function of pump fluence for both linear and circular polarization; these experiments are fast and

the temporal stability of the laser is then sufficient to monitor highly nonlinear transient signal versus the pump power.

2. Measurements of transient waveforms $\Delta E(\tau;\tau_p)$ with a fixed pump–probe delay τ_p (to 5, 10, 60, 300 ps) for selected pump fluences. These experiments mainly probe the photogenerated electron plasma dynamics, e.g., they connect the previously determined $\Delta E_{\max}$ to the actual free electron density N_{e}. In order to enable quantitative extraction of plasma characteristics and the related optical constants, the measurements are supplemented with equilibrium reference waveforms $E(\tau)$ obtained with the optical pump blocked.

3. Pump-probe scans where the time τ was fixed at the maximum of the transient waveform and τ_p was varied.

3 Experimental results and discussion

The THz probing radiation is very sensitive to the presence of mobile free carriers. It is, therefore, expected to interact strongly with the free electron plasma generated by photo-ionization of oxygen molecules. Indeed, the plasma frequency of free electron gas falls into the sub-THz range for the free electron densities around $10^{14} - 10^{15}$ cm^{-3}. The ionized oxygen molecules themselves are much heavier and their translational motion cannot be efficiently driven by the THz field. The transient THz signal measured in our experiments will thus primarily reflect the rate of photoionization (through the electron density monitoring), the subsequent plasma expansion and the scattering rate of the free electrons. In addition, rotational fingerprints of some products of chemical interactions triggered by the optical excitation can be possibly detected.

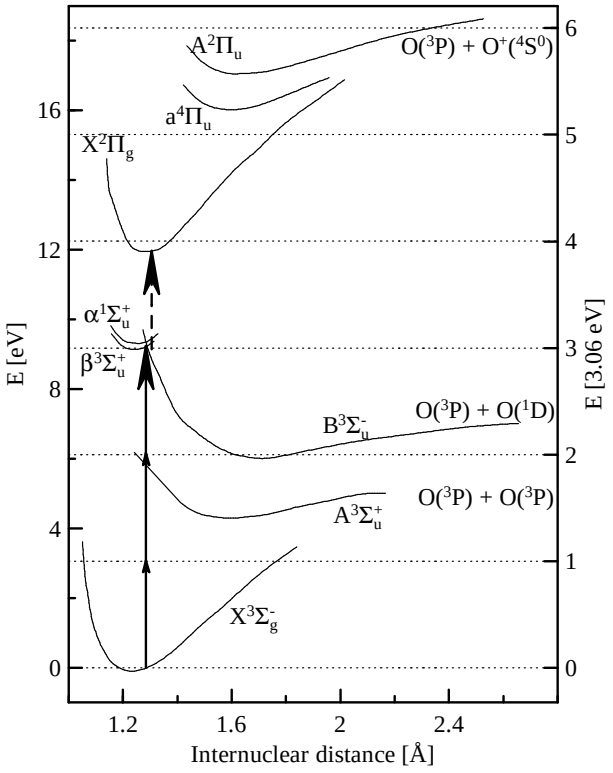

Figure 2: Potential curves of O_2 and O_2^+ with the most probable multiphoton excitation and ionization process at 405 nm denoted by arrows. The right-hand scale is normalized by the energy of 405 nm photons, i.e., it indicates the number of blue photons needed for a particular transition. Full arrow indicates the first resonant step, the dashed arrow indicates the second step involving the photoionization of the oxygen molecule.

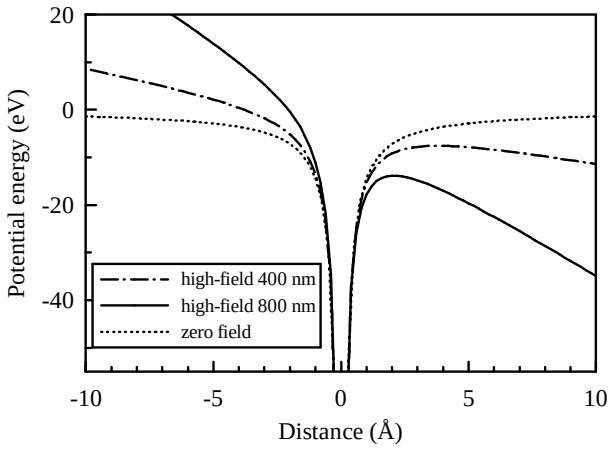

Figure 3: Schematic picture of the influence of the laser electric field on the Coulomb potential due to the positively charged core felt by the electron in the static approximation. The maximum available values of the electric field for both experimental wavelengths were assumed in the plot.

In section 3.1, we show selected experimental results, which alone provide an instructive picture of the probed processes. Subsequently, we discuss and quantitatively analyze the most prominent features in the transient dielectric spectra which are attributed to the plasma dynamics. Finally, a more detailed analysis of the spectra allows us to identify other involved chemical processes.

3.1 Photo-ionization processes in oxygen

We use two pump wavelengths (810 and 405 nm) which are expected to invoke qualitatively different ionization processes. The character of the ionization process in an intense laser field can be estimated using the Keldysh parameter γ which reads[45, 46]

$$\gamma = \omega \sqrt{\frac{E_\mathrm{B}}{I}} \sqrt{\frac{m_e}{z_0 e^2}} \tag{1}$$

in SI units; E_B is the ionization potential, I is the laser pulse intensity, m_e is the electron mass, $z_0 = 377\,\Omega$ is the vacuum wave impedance, and e is the electron charge. A multiphoton ionization regime corresponds to $\gamma \gg 1$, while the strong-field tunneling process becomes dominant for $\gamma \lesssim 1$.

The adiabatic ionization potential of O_2 is $E_\mathrm{B} = 12.07\,\mathrm{eV}$,[47] which corresponds to about four quanta of our blue pump radiation (405 nm $\approx$ 3.06 eV). The Keldysh parameter for the highest pump intensities used at this wavelength (15.5 TW/cm^2) is $\gamma \approx 5.5$. Fig. 2 schematically shows a partial potential energy diagram for neutral oxygen molecule and for its cation and the ionization pathways which can be considered in our experiments. A resonantly enhanced $(3+1)$-photon process passing through the Schumann-Runge system $X^3\Sigma_g^- \rightarrow B^3\Sigma_u^-$, which is the strongest absorption band of oxygen, is the most probable.[47] This process also leads to dissociation of a significant fraction of oxygen molecules with subsequent formation of ozone.

Note that the resonant enhancement via two-photon absorption in the Herzberg band $X^3\Sigma_g^- \rightarrow A^3\Sigma_u^+$ is symmetry forbidden.

Excitation with a 810 nm ($\approx$ 1.53 eV) radiation would require a minimum absorption of eight photons to ionize oxygen in a multiphoton process, which is a quite improbable process for the pump fields used. For these experiments with a linearly polarized pump pulse a strong-field tunneling ionization is expected to dominate (see Fig. 3) in agreement with the value of the Keldysh parameter for the highest pump fluences (150 TW/cm^2), $\gamma \approx 0.8$. Moreover, for a sufficiently strong driving field the Coulomb potential attracting the valence electrons can be entirely suppressed, i.e. there is a critical optical field which allows the bound electron to escape without tunneling.[48] Assuming a quasi-static approximation and considering the effective ionic charge acting on the valence electron $Z = 1$ the threshold intensity leading to the Coulomb barrier suppression in our experiments can be estimated to be $I_{\mathrm{th}} \approx 85\,\mathrm{TW/cm^2}$.

In contrast, the strong-field effects are expected to be much less efficient for the circularly polarized pump light which drives the bound electrons on circular orbits.[1] In addition, for small linear molecules like O_2, a rapid molecular alignment with the laser polarization can occur due to the torque on the laser-induced dipole moment. This alignment is only possible in a linearly polarized light.[49] Structure-based calculations of the ionization tunneling show an enhancement of the ionization rate when the long axis of the molecular potential is aligned with the laser field.[50, 51] With regard to these mechanisms, comparative experiments with linearly and circularly polarized pump light can distinguish between multiphoton and strong-field ionization mechanisms.

Fig. 4 shows a compilation of results related to the pump intensity dependence of the transient THz signal shortly ($\tau_p = 10\,\mathrm{ps}$) after photoexcitation. At this stage we can comment

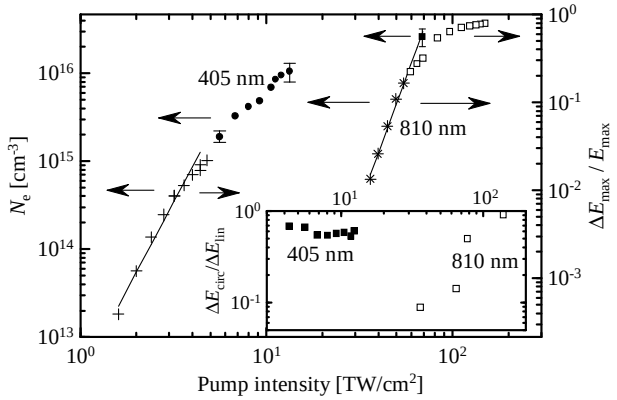

Figure 4: Compilation of results showing the transient THz signal and free electron density versus pump intensity (linear polarization). Stars and crosses: both vertical scales are relevant; filled symbols: only left-hand scale is relevant, open symbols: only right-hand scale is relevant (as shown by the arrows). Inset: measured ratio between the transient THz signal for circularly and linearly polarized pump.

on the results related to the right-hand vertical scale only (the method of the evaluation of the plasma density N_e from the transient spectra will be shown later in detail). However, even these raw results provide a clear picture of the ionization processes. A net intensity gap is observed between the signal measured for 405 nm and that obtained for 810 nm. The slopes of the increase of the transient THz signal versus the pump intensity are also significantly different. The data obtained for the blue pump and with $I < 5\,\mathrm{TW/cm^2}$ can be approximately fitted by a I^4 dependence. For the 810 nm pump, the slope in the low-intensity regime equals roughly to six. For intensities above 75 TW/cm^2 a dielectric breakdown occurs accompanied by a white-light continuum generation in the focal spot.[18] Note that this intensity threshold closely matches the value of 85 TW/cm^{-1} expected for the Coulomb barrier suppression in the quasi-static limit (see above).

To distinguish between multiphoton and high-field ionization mechanisms we carried out comparative experiments with linearly and circularly polarized pump light. Both polarizations should approximately equally contribute to the multiphoton ionization process, while the circular one is assumed to be much less efficient for the strong-field tunneling process. The difference

in the THz signal induced by the two different pump polarizations then provides the information about the extent of the strong-field process (see inset of Fig. 4). For 405 nm, $\Delta E_{\mathrm{circ}}/\Delta E_{\mathrm{lin}}$ is about 0.6–0.7 for a broad range of pump intensities. The multiphoton character of the ionization process is dominant, but the strong-field process is not negligible in agreement with the magnitude of the Keldysh parameter ($\gamma \approx 5.5$). In contrast, at 810 nm, $\Delta E_{\mathrm{circ}}/\Delta E_{\mathrm{lin}} \approx 0.1$ at 35 TW/cm^2: clearly the strong-field ionization is a dominant effect. For higher values of I, $\Delta E_{\mathrm{circ}}/\Delta E_{\mathrm{lin}}$ comes closer to one; this is due to the saturation of the THz absorption rather than to a change of ionization mechanism.

Fig. 5 shows an example of pump–probe scans for both pump wavelengths and using the linear polarization of the pump beam. For these measurements the delay time τ was fixed to the value ΔE_{max} for which the transient signal $\Delta E(\tau)$ reaches its maximum and the delay time τ_p was scanned. The data shown in Fig. 5 were measured using such pump powers that the normalized signal $\Delta E_{\mathrm{max}}/E_{\mathrm{max}}$ reaches similar values for both pump wavelengths. Note that the ratio between these two pump intensity values is about 6, which indicates much stronger ionization effects induced by the blue pump.

As expected, the transient signal shows a sharp rise at zero pump–probe delay. For higher pump–probe delays a signal plateau is observed which extends over about 100 ps for the blue pump. The plateau is followed by an exponential decay with a time constant of $\approx$ 300 ps. The same shape of the signal is observed also for lower pump intensities than those reported in Fig. 5. The very slow pump–probe dynamics observed gives us the possibility to calculate the dielectric spectra of the plasma from individual transient waveform scans by means of a simple Fourier transformation without any loss of information.[43, 44]

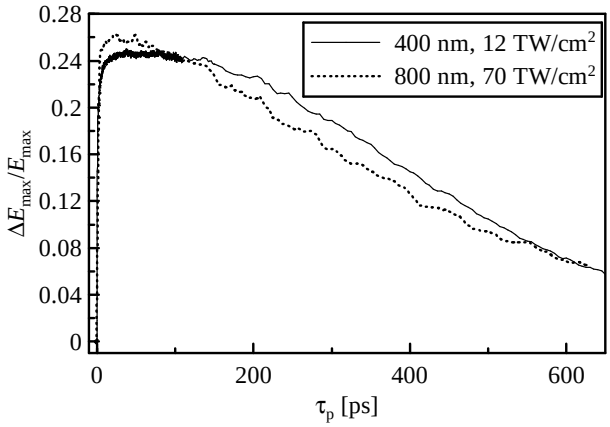

Figure 5: Pump–probe scans: maximum field amplitude of the transient signal normalized by the maximum field amplitude of the reference waveform versus pump–probe delay.

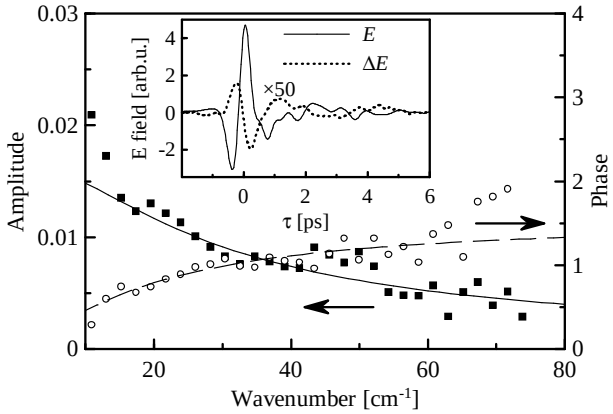

Figure 6: Transient field transmittance $\Delta t(\omega)$ at low pump intensity and the best fit using Drude model; pump wavelength: 405 nm; pump intensity: 3.2 TW/cm^2; pump–probe delay: $\tau_p = 10$ ps. Inset: corresponding equilibrium $E(\tau)$ and transient $\Delta E(\tau, \tau_p)$ waveforms.

3.2 Transient dielectric spectra

We have shown (Fig. 5) that the temporal evolution of the pump–probe signal is much slower than the probing THz pulse length. Consequently, the transient dielectric spectra of the photo-excited gas can be directly calculated from the waveforms measured at a fixed pump–probe delay. The inset in Fig. 6 shows an example of the equilibrium $E(\tau)$ and transient $\Delta E(\tau; \tau_p)$ waveforms obtained with 3.2 TW/cm^2 pump power at 405 nm and with $\tau_p = 10\,$ps. The reverse sign of the transient field accounts for the fact that the THz field transmitted through the photo-generated plasma is lower than that obtained in equilibrium. The corresponding

transient transmission spectrum can obtained by a Fourier transformation of the waveforms:

$$\Delta t(\omega) = \Delta E(\omega; \tau_p)/E(\omega)\,. \tag{2}$$

Obviously, the induced changes in the transmitted THz waveform (Fig. 6) are very small for the experimental conditions used here, however, they are expected to increase with increasing pump intensity. It can be shown that the transmission through the photo-excited volume can be within a good approximation analyzed using the formula for the complex transmittance of a thin slab. A careful analysis of the experimental geometry close to the interaction volume yields (see Appendix B):

$$\Delta t(\omega) = \{\exp[i\omega(n + i\kappa)d_{\mathrm{eff}}/c] - 1\}\frac{V}{d_{\mathrm{eff}}S_{\mathrm{a}}}\,, \tag{3}$$

where $S_{\mathrm{a}} = 0.5\,\mathrm{mm}$ is the opening of the metallic aperture at the pump beam focus, $d_{\mathrm{eff}} \approx 180\,\mu\mathrm{m}$ is the effective THz beam path through a cylindrical interaction volume $V \approx 0.005\,\mathrm{mm}^3$, and $\Delta N = n + i\kappa$ is the pump-induced change of the complex refractive index related to the transient dielectric spectrum $\varepsilon(\omega)$ by:

$$\varepsilon(\omega) = (1 + \Delta N(\omega))^2\,. \tag{4}$$

For the lowest pump intensities, as long as $\Delta E \ll E$, the exponential term in (3) can be developed into a truncated series. Within this approximation the transient transmittance scales linearly both with ΔN and with the interaction volume V

$$\Delta t = \frac{\omega}{c}(in - \kappa)\frac{V}{S_{\mathrm{a}}}\,. \tag{5}$$

3.2.1 Plasma oscillations

A series of transient THz waveforms was measured with the blue linearly polarized pump beam at $\tau_p = 10$ ps for pump intensities ranging from 3.2 to 13.3 TW/cm^2 (Figs. 7 and 8). The

spectrum at $I = 3.2\,\mathrm{TW/cm^2}$ corresponds to the transmission function and waveforms plotted in Fig. 6.

To describe the motion of the electrons and interpret the measured dielectric spectra, we use a simple Drude-Lorentz model.[52] The time dependence of the average electron velocity is in the Drude-Lorentz picture given as

$$\frac{dv(t)}{dt} + \frac{v}{\tau_s} = -\frac{e}{m_\mathrm{e}} E_\mathrm{loc}\,, \tag{6}$$

where τ_s is the momentum scattering time, m_e is the electron mass, and $-e$ is its charge. E_loc is the local electric field acting on the charges. For a homogeneous plasma it is equal to the incident THz field E. In this case we obtain the usual Drude formula,[52]

$$\varepsilon(\omega) = 1 - \frac{\omega_p^2}{i\omega/\tau_s + \omega^2}\,, \tag{7}$$

where ω_p is the plasma frequency depending on the free electron density N_e as $\omega_p^2 = N_e\, e^2/(\varepsilon_0 m_\mathrm{e})$. However, we deal with the situation where, at early times after photo-ionization (when the diffusion process can still be neglected) the electron-ion plasma is localized within a cylinder much narrower than the probing beam waist. In this case, application of the THz field may lead to an effective spatial separation of charges resulting in a dynamical screening of the applied field. Let P be the space-charge polarization due to the charge carriers separating in the field. The local field then reads:[53]

$$E_\mathrm{loc} = E - \frac{P}{2\varepsilon_0}\,, \tag{8}$$

where the numerical factor 2 comes from the fact that the plasma is localized in a cylindrical region nearly perpendicular to the probing THz field. The rate of change of the screening polarization is related to the electron current density:

$$\frac{dP}{dt} = -eN_e v\,, \tag{9}$$

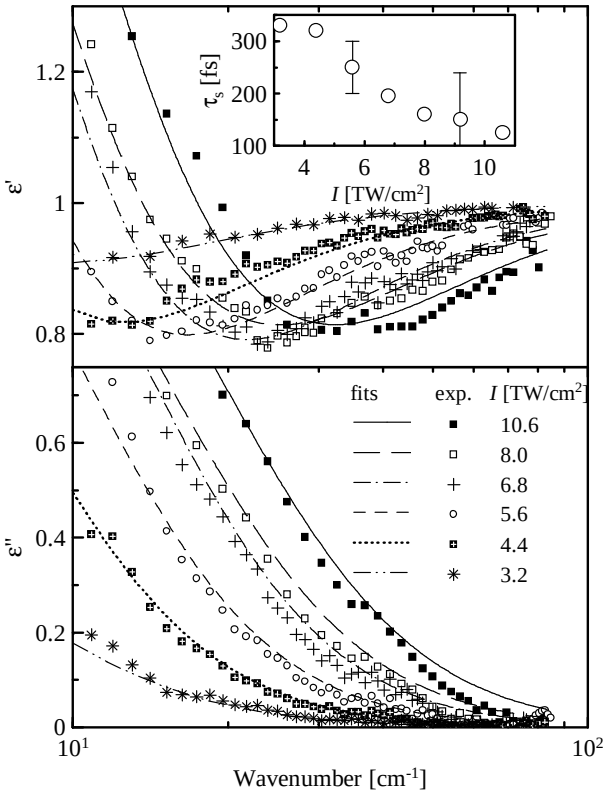

Figure 7: Dielectric spectra of electronic plasma in photo-ionized oxygen calculated from transient waveforms using Eq. (3) and the fits by the Drude-Lorentz model (10) for several pump pulse intensities. Optical pump at 405 nm, linearly polarized, $\tau_p = 10$ ps. Inset: momentum relaxation time τ_s extracted from the fits.

Putting together equations (6), (8) and (9) one obtains

$$\varepsilon(\omega) = 1 - \frac{\omega_p^2}{i\omega/\tau_s + \omega^2 - \omega_p^2/2}\,. \tag{10}$$

It follows from this equation that, for sufficiently long scattering times τ_s (underdamped plasma), THz plasma oscillations at the frequency $\omega_p/\sqrt{2}$ can be directly observed due to the carrier screening effects.

Note also that for low pump intensities ΔN yielded by Eq. (10) is proportional to N_e and the transient THz spectrum described by Eq. (5) is then proportional to the total number of free electrons in the interaction volume.

The transient dielectric spectra of the plasma (shown in Fig. 7) are marked by a classical Drude behavior in the high frequency part and by oscillations due to the charge separation at

lower frequencies. The presence of these oscillations is reflected in the anomalous dispersion character of the real part of the permittivity. A very good agreement between the data and the fits by formula (10) is obtained for pump intensities up to 10 TW/cm^2 (data shown in Fig. 7). Only semiquantitative agreement can be obtained for higher pump intensities (an example is shown in Fig. 8). We attribute this fact to the scattering of the THz light on inhomogeneous highly concentrated plasma. In other words, the approximation leading to Eq. (3) reaches the limits of its validity for these experimental conditions.

The fits of the transient spectra yield the pump intensity dependence of the momentum scattering time τ_s (see inset of Fig. 7) and of the plasma density N_e. This last result allows us to plot the left vertical scale in Fig. 4 and to obtain a more quantitative picture of the carrier densities involved in different regimes of photo-ionization. Strictly speaking, Fig. 4 gives the plasma density after the geminate recombination process.

To check the robustness of the fits we calculated and fitted trial spectra where d_eff and V were varied by 20%. These fits lead to a slightly different values of τ_s, while they did not have any influence on the value of N_e. An attempt to analyze the measured raw spectra with the linear approach described by Eq. (5) leads to practically identical results for $I \leq 4.4\,\mathrm{TW/cm^2}$, which means that for these intensities the transient signal is proportional to the total number of electrons probed by the THz field. For higher intensities the plasma induced changes of the dielectric properties are overestimated when Eq. (5) is used for the data analysis. Nevertheless, even for such data, the fit by Eq. (10) leads to the same values of N_e as those obtained using Eq. (3). The experimental values of N_e (see Fig. 4) thus seem to be quite well defined by the position of the increase of the real part of the permittivity and are not significantly influenced by the experimental parameters that were estimated only approximately from the

experimental geometry (see Appendix B). The values of τ_s (see inset of Fig. 7) show some spread upon modification of experimental parameters; its extent is shown by error bars in the figure. However, the general trend characterized by a decrease of τ_s upon raising the pump pulse intensity is preserved for all the fits.

As the concentration of free electrons N_e and of ionized oxygen molecules is about three to five orders of magnitude lower than that of neutral molecules (N_0), the dominating scattering process for free electrons is that on neutral molecules.[54] The momentum scattering time τ_s of free electrons is equal to:

$$\tau_s = \frac{1}{\sigma N_0 v_e} \tag{11}$$

with $\sigma \approx 10^{-19}\,\mathrm{m}^2$ denoting the electron momentum scattering cross-section for neutral oxygen molecules,[55] $N_0 = 2.7 \times 10^{19}\,\mathrm{cm}^{-3}$ is the concentration of oxygen molecules at atmospheric pressure and v_e is the thermal electron velocity. The typical electron excess energies achievable in our experiments are units of eV, leading to initial electronic velocities of the order of $v_e \sim 10^6\,\mathrm{m/s}$. In this case Eq. (11) yields $\tau_s \approx 350\,\mathrm{fs}$ and provides a semiquantitative agreement with the values obtained in our experiments. Even for the blue excitation, which was shown to be dominated by multi-photon ionization process, the strong field effects are not entirely negligible ($\Delta E_\mathrm{circ}/\Delta E_\mathrm{lin} \approx 0.6$). The increase of the scattering rate with increasing pump intensity observed in the inset of Fig. 7 then can be attributed to the deformation of the Coulomb potential in the strong field of the pump pulse and the related increase of the electron excess energy for the four-photon ionization process.

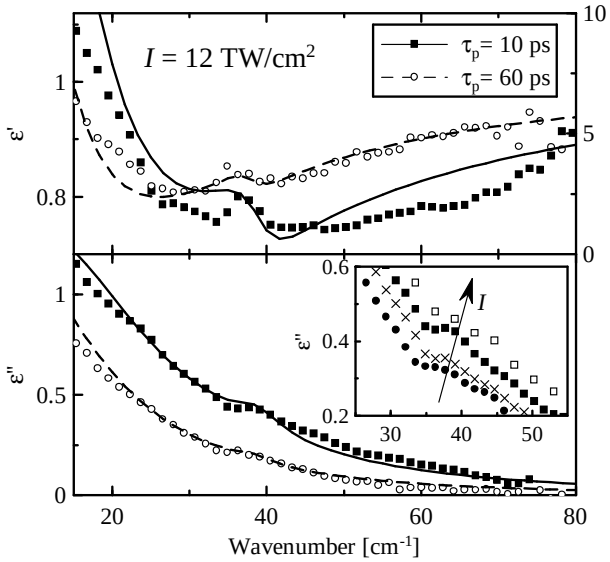

Figure 8: Transient dielectric spectra obtained for $I = 12\,\mathrm{TW/cm^2}$ and two different pump–probe delays $\tau_p = 10$, 60 ps and their fits using the Drude-Lorentz model (10) superposed with an underdamped harmonic oscillator at 39 $\mathrm{cm^{-1}}$ ($\tau_p = 10\,\mathrm{ps}$) and at 38 $\mathrm{cm^{-1}}$ ($\tau_p = 60\,\mathrm{ps}$). See the text for details. Inset: Imaginary part of the permittivity for several pump fluences (10.5–13.2 $\mathrm{TW/cm^2}$) at $\tau_p = 10\,\mathrm{ps}$.

3.2.2 Plasma expansion

Fig. 9 shows examples of transient transmission functions obtained for several pump–probe delays. Let us focus our attention to the pump–probe scans shown in Fig. 5, as well as to the spectra obtained for a variable pump–probe delay (Figs. 9 and 8).

We have already pointed out that for low pump intensities the transient THz signal is proportional to the total number of electrons probed by the THz field. It means that for early time delays τ_p where the plateau is observed in the pump–probe scan of $\Delta E_{\max}$ this number remains constant. The signal is governed by the diffusion of carriers within the diaphragm clear aperture. The temporal extent of the plateau then corresponds to the time the electrons need to escape from the probed volume and/or it may be comparable to the electron–ion recombination time which would also lead to a decrease of the total number of the probed carriers.

The origin of the plateau in the pump–probe scans (see Fig. 5) for high pump intensities

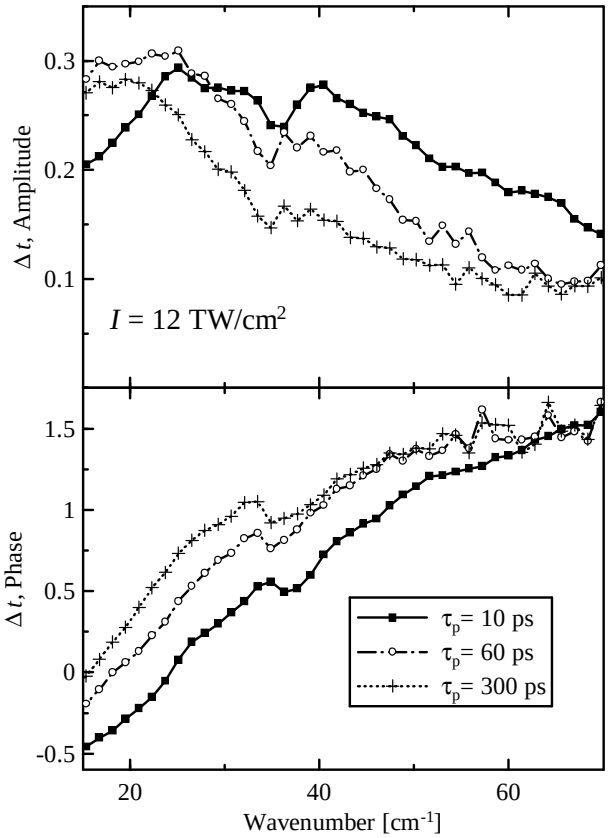

Figure 9: Transient field transmittance spectra $\Delta t(\omega)$ at $I = 12\,\mathrm{TW/cm^2}$ for the pump wavelength of 405 nm and for three significantly different pump–probe delays τ_p.

($I > 4.4\,\mathrm{TW/cm^2}$) can be understood from Fig. 9 where the transient transmission spectra are shown for 12 TW/cm^2 pump intensity at several pump–probe delays. At early times after photo-ionization, the electron plasma is dense and confined to a rather small volume. In these conditions, the electron plasma density amounts $\approx 10^{16}\,\mathrm{cm^{-3}}$ and the plasma frequency $\omega_p/(2\pi) \approx 30\,\mathrm{cm^{-1}}$. Note that the excitation of the transverse plasma oscillations by the THz field at $\tau_p = 10\,\mathrm{ps}$ is clearly observed as a decrease of the transient transmission around $\omega_p/(2\sqrt{2}\pi) \approx 21\,\mathrm{cm^{-1}}$. Subsequently, a plasma expansion in the radial direction (with respect to the direction of the pump beam propagation) occurs leading to the reduction of the electron density. However, the sample is not in the linear regime described by Eq. (5); consequently, the transient spectrum must change its shape. The transverse plasma oscillations are shifted

to lower frequency and the high-frequency part of the transient signal is reduced (cf. Fig. 9). The total number of probed free electrons being still conserved we come to the conclusion that, in this regime, the product $N_e d_{\mathrm{eff}}^2$ remains constant.

In order to evaluate the rate of expansion, we have calculated several trial dielectric spectra from the transmission function obtained at $\tau_p = 60\,\mathrm{ps}$ (open circles in Fig. 9) inserting different values of $d_{\mathrm{eff}}(60\,\mathrm{ps}) = k d_{\mathrm{eff}}$ into Eq. (3). Subsequently we tried to fit those trial spectra with the Drude-Lorentz model, where the electron density was fixed to the expected value $N_e(60\,\mathrm{ps}) = N_e/k^2$. We find that a very good fit is obtained for $k \approx 1.4$ (see Fig. 8); in agreement with this, the scattering time is found to be increased by about 30%. This corresponds to an effective radial velocity of expansion of $1.6 \times 10^5\,\mathrm{m/s}$.

3.3 Rotational lines in the spectra

Rotational spectral lines of ozone at 21.9 cm^{-1} and 28 cm^{-1} [56] were observed both in reference (pump beam off) and in transient (pump beam on) THz spectra. Strictly speaking, these lines were not observed immediately after the experimental chamber was filled by fresh oxygen but after a sufficiently long optical pumping. This demonstrates the pump-induced formation and long-lived presence of the molecules of O_3 in the experimental chamber. As the path of the THz beam is rather long in the chamber (60 cm) already a relatively low concentration of O_3 can lead to a measurable effect. However, we emphasize that this is not a transient effect, these lines are not directly related to each pump event, but rather to a cumulative effect of a long exposition to the intense beam. Indeed, these lines were observed in the waveforms obtained with the pump beam on as well as in those obtained with the pump beam off so that the transient spectra obtained by their ratio do not contain their signature.

In contrast to these quasi-equilibrium spectral lines, a marked transient feature is observed at about 39 cm^{-1} for the pump intensities higher than 8 TW/cm^2. This line is observed both in amplitude and phase spectra (see Figs. 8 and 9); its shape evokes an oscillatory mode with a lifetime exceeding 300 ps. Its contribution to the transient dielectric spectra can be fitted by an underdamped harmonic oscillator mode at 39 cm^{-1} for $\tau_p = 10\,ps$ and at 38 cm^{-1} for $\tau_p = 60\,ps$ and $\tau_p = 300\,ps$. We believe that this line cannot be directly related to the electron plasma dynamics which is as a rule strongly dependent on the free charge density. Indeed, the position of this line is only very weakly dependent on the pump pulse intensity (see inset of Fig. 8). The evolution of the plasma contribution (i.e., the whole transmission function less the feature around 39 cm^{-1}) upon increasing the pump–probe delay is clearly marked in the spectra by a net vertical scaling of the transmission function and by significant changes of its shape below 25 cm^{-1} (Fig. 9). In contrast, the line at 39 cm^{-1} does not change its shape and exhibits only a very small red-shift at early times.

We have searched for a possible molecular origin of this line. Gaseous impurities, such as water vapor, could be possibly responsible for the 39 cm^{-1} spectral feature. Note that this feature is very close to a prominent water molecule rotational line.[47] Moreover, simple ab initio calculations (at the MP2/aug-cc-pvtz level) show that H_2O^+ has almost the same geometry (and thus also rotational spectrum) as H_2O and that it has about 15 % larger dipole moment than a neutral water molecule. Therefore, H_2O^+, if formed in the experiment, would show a strong rotational line around 39 cm^{-1}. However, it is not clear, why other water lines (e.g., at about 47 cm^{-1} and 55.5 cm^{-1}, which exhibit even a stronger absorption in equilibrium water vapor transmission measurements) are not observed. It is also possible that the discrepancy between the experimental data and the fit in the spectral range 45–70 cm^{-1} for $\tau_p = 10\,ps$ observed in

Fig. 8 is due to a more complex spectral feature consisting of several strongly damped lines.

As described above, ozone is formed in the chamber during the experiment. The "non-plasma" spectral feature could possibly also come from rotation of a transient O_3^+ ion. This ion can be most likely formed via secondary ionization of ozone. The lifetime of ozone cation should be very short since it can readily neutralize by electron capture and/or react chemically. Since the geometry of O_3^+ is less bent than that of ozone (O-O-O angle of 133.6° for the former and 116.8° for the latter species) its largest rotational constant is almost twice that of O_3 (rotational constants of ozone cation evaluated at the MP2/cc-pvqz level are 6.595, 0.403, and 0.380 cm^{-1}). Ozone cation should thus exhibit strong rotational line around 31 and 43 cm^{-1}. These are the $K = 2 \rightarrow 1$ and $K = 3 \rightarrow 2$ lines within the near-prolate top approximation.[47] Our estimates are in a good agreement with the results of a most recent comprehensive study of the rotational structure in the spectra of photoionized ozone. [57] They are, however, somewhat short of a perfect match with the present experiment.

In summary, is is likely that the transient feature around 39 cm^{-1} is a rotational signature of a molecular ion such as H_2O^+ or O_3^+, but firm evidence is still elusive.

4 Conclusion

We have applied optical pump—THz probe spectroscopy to the investigation of ionization mechanisms in oxygen gas. We have elucidated two different mechanisms of plasma formation: strong-field ionization (Keldysh parameter $\gamma \approx 1$) pertinent to 800 nm pumping and multiphoton ionization ($\gamma \gtrsim 5$) dominating at 400 nm. We have characterized the oscillatory dynamics and diffusion of free electron plasma. Plasma oscillations were clearly identified in the spectra yielding plasma densities in the range $10^{13} - 10^{16} cm^{-3}$ and sub-ps momentum scattering times,

based on the Drude-Lorentz model adapted for inhomogeneous plasma. In the present plasma, which is formed by a weakly ionized gas, diffusion on the sub-ns scale dominates over recombination. We have also detected rotational signatures of stationary and transient molecular and ionic species.

Appendix A: Control of the pump pulse intensity

A considerable attention has been paid to a precise control of the pump pulse intensity in the experiments. In particular, specific experimental schemes were set up to allow for its smooth variation by the rotation of a single plane parallel zero-order half-wave plate. These schemes made it possible to measure the power dependence of the transient THz signal with a small power step, while keeping the pump–probe delay constant and avoiding significant changes of other important pump pulse characteristics. These schemes are shown in Fig. 10.

In the experiments with 405 nm pump control was achieved using the polarization selectivity of the second harmonic generation process (see panel (a) of Fig. 10). The orientation of the $\lambda/2$-plate controls the intensity of the vertically polarized second harmonic wave over about an order of magnitude. Switching between two positions of the tunable retardation plate (RP) then enables pumping with either linearly or circularly polarized light. The SHG stage was well separated from the THz spectrometer so that no possible optically rectified signal from the LBO crystal[40] could come into the THz detection system.

For experiments with 810 nm the pump intensity tuning was achieved using the polarization selectivity of the reflection at the Brewster angle (panel (b) of Fig. 10). If, in addition, a thin (0.5 mm) gray filter was inserted into the beam path, a smooth control of the light intensity over nearly an order of magnitude was achieved for the linearly polarized pump beam. We

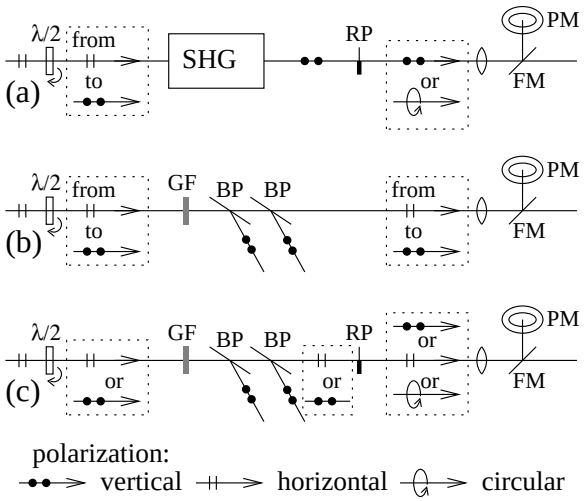

Figure 10: Transformation of the pump beam in view of the intensity scaling for the two polarizations used. Pumping with (a) 405 nm, linear or circular polarizations; (b) 810 nm, linear polarization; (c) 810 nm, linear or circular polarizations. $\lambda/2$: half-wave plate, SHG: second harmonic generation, RP tunable retardation plate, BP: Brewster plate, GF: thin gray filter, FM: flipping mirror, PM: power meter.

estimate that the increase of the pump pulse length due to the insertion of the filter can be neglected. Note, however, that only four cleanly defined experimental points could have been obtained for the direct comparison between the linearly and circularly polarized pump at 810 nm (panel (c) of Fig. 10).

Appendix B: Determination of the dielectric spectra

In this part we discuss the method used for the spectral analysis of experimentally obtained waveforms. We describe the evaluation of the dielectric spectra from the measured transient transmission function. An example of the experimentally obtained transmission function is shown in Fig. 6. These are the raw data. It is now possible to show that the transmission through the photo-excited volume can be within a good approximation analyzed using the formula for the complex transmittance of a thin slab.

Here we deal with highly non-linear processes for which the estimation of the effective in-

teraction volume V is not unambiguous mainly owing to the fact that the pump beam profile is not homogeneous.[46] The optical and THz beams intersect in the volume with an approximately cylindrical shape (see inset of Fig. 1). The main part of the transient signal at early times after photo-excitation will obviously come from the central region of this volume where the laser intensity reaches the highest values. For the 405 nm pump wavelength, we deal essentially with four-photon processes. Therefore we consider the half-width of the radial profile of I^4 as a good approximation of the radius r of the cylindrical interaction volume; this leads to $V \approx 0.005\,\mathrm{mm}^3$. The average path of the THz probing wave through this cylinder can be then considered as an effective thickness d_{eff} of the plasma. Simple geometrical analysis shows that $d_{\mathrm{eff}} = \pi r/(2\sin\alpha) \approx 180\,\mu\mathrm{m}$.

The THz properties of the sample (represented by the photo-excited volume) can be accounted for by a complex refractive index $N = 1 + \Delta N$, where $\Delta N = n + i\kappa$ describes the photo-induced change. The transient transmittance spectrum $\Delta t(\omega)$ of the sample is then approximately described by the following function:

$$\Delta t = [t_{\mathrm{F}} \exp(i\omega \Delta N d_{\mathrm{eff}}/c) - 1]\frac{S_{\mathrm{eff}}}{S_{\mathrm{a}}} \tag{12}$$

where t_{F} formally accounts for the transmission losses due to interfaces (for a homogeneous sample it would be the Fresnel transmission coefficient) and c denotes the vacuum speed of light. The effective input surface of the sample is $S_{\mathrm{eff}} = V/d_{\mathrm{eff}}$; S_{a} denotes the free surface of the aperture. The exponential term describes the phase change and the absorption due to the propagation through the plasma. We assume that the optical constants of the excited region are very close to equilibrium ($n \approx 0$, $\kappa \approx 0$). The Fresnel transmission coefficient of a homogeneous slab with such optical constants is very close to unity; one finds $t_{\mathrm{F}} \approx 0.998$ for $\Delta N \approx 0.1$ and $t_{\mathrm{F}} \approx 0.96$ for $\Delta N \approx 0.5$. It means that the transmission changes due to inhomogeneities (i.e.,

partial reflections, scattering) can be neglected compared to those related to the propagation effects described by the exponential term. Thus, for our quantitative analysis of the transient waveforms we use the following formula:

$$\Delta t = \{\exp[i\omega(n + i\kappa)d_{\mathrm{eff}}/c] - 1\}\frac{V}{d_{\mathrm{eff}}S_{\mathrm{a}}}\,. \tag{13}$$

One has to bear in mind that the evaluation of the optical constants of the excited gas relies on our choice of the interaction volume which cannot be unambiguously defined. Nevertheless an excellent agreement of our experimental data with the fits by the Drude-Lorentz model presented in the main part of the paper justifies to a large extent this choice.

Acknowledgment

Support from the Czech Ministry of Education (grant LC512) is gratefully acknowledged. Part of the work was supported via the Research Project Z40550506. One of us (SEB) is supported by the National Science Foundation (grant CHE-0311814) and the David and Lucile Packard Foundation.

References

[1] P. B. Corkum, *Phys. Rev. Lett.* **71**, 1994 (1993).

[2] R. R. Alfano, *The Supercontinuum Laser Source, 2nd edition*, Springer, Berlin (2005).

[3] M. Lewenstein, P. Balcou, M. Y. Ivanov, A. L'Huilier, and P. B. Corkum, *Phys. Rev. A* **49**, 2117 (1994).

[4] P. Antoine, A. L'Huilier, and M. Lewenstein, *Phys. Rev. Lett.* **77**, 1234 (1996).

[5] I. P. Christov, M. M. Murnane, and H. C. Kapteyn, *Phys. Rev. Lett.* **78**, 1251 (1997).

[6] I. P. Christov, M. M. Murnane, and H. C. Kapteyn, *Phys. Rev. A* **57**, R2285 (1998).

[7] R. Srinivasan and B. Braren, *Chem. Rev.* **89**, 1303 (1989).

[8] L. J. Radziemski, *Microchem. Journal* **50**, 218 (1994).

[9] E. N. Glezer and E. Mazur, *Appl. Phys. Lett.* **71**, 882 (1997).

[10] C. B. Schaffer, A. Brodeur, and E. Mazur, *Meas. Sci. Technol.* **12**, 1784 (2001).

[11] M. D. Perry and G. Mourou, *Science* **264**, 917 (1994).

[12] Z. G. Lu, P. Campbell, and X.-C. Zhang, *Appl. Phys. Lett.* **71**, 593 (1997).

[13] T. Ditmire, J. Zweiback, V. P. Yanovsky, T. E. Cowan, G. Hays, and K. B. Wharton, *Nature* **398**, 489 (1999).

[14] R. Rankin, C. E. Capjack, N. H. Burnett, and P. B. Corkum, *Opt. Lett.* **16**, 835 (1991).

[15] N. Akozbek, A. Becker, and S. L. Chin, *Laser Phys.* **15**, 607 (2005).

[16] Y. B. Zel'dovich and Y. P. Raiser, *Sov. Phys. JETP* **20**, 772 (1965).

[17] G. A. Askaryan and M. S. Rabinovich, *Sov. Phys. JETP* **21**, 190 (1965).

[18] A. V. Benderskii, R. Zadoyan, N. Schwentner, and V. A. Apkarian, *J. Chem. Phys.* **110**, 1542 (1999).

[19] M. Petterson, R. Zadoyan, J. Eloranta, N. Schwentner, and V. A. Apkarian, *J. Phys. Chem. A* **106**, 8308 (2002).

[20] D. M. Rayner, A. Naumov, and P. B. Corkum, *Optics Express* **13**, 3208 (2005).

[21] L. N. Gaier, M. Lein, M. I. Stockman, G. L. Yudin, P. B. Corkum, M. Y. Ivanov, and P. L. Knight, *J. Mod. Optics* **52**, 1019 (2005).

[22] S. P. LeBlanc, R. Sauerbrey, S. C. Rae, and K. Burnett, *J. Opt. Soc. Am. B* **10**, 1801 (1993).

[23] S. C. Rae and K. Burnett, *Phys. Rev. A* **46**, 1084 (1992).

[24] B. M. Penetrante, J. N. Bardsley, W. M. Wood, C. W. Siders, and M. C. Downer, *J. Opt. Soc. Am. B* **9**, 2032 (1992).

[25] E. Gibson, A. Paul, N. Wagner, R. Tobey, D. Gaudiosi, S. Backus, I. Christov, A. Aquila, E. Gullikson, D. Attwood, M. M. Murnane, and H. C. Kapteyn, *Science* **302**, 95 (2003).

[26] S. Champeaux and L. Berge, *Phys. Rev. E* **71**, 046604 (2005).

[27] A. Petrignani, W. J. V. D. Zande, P. C. Cosby, F. Hellberg, R. D. Thomas, and M. Larsson, *J. Chem. Phys.* **122**, 014302 (2005).

[28] E. C. Zipf, *J. Geophys. Res.* **85**, 4232 (1980).

[29] B. D. Sharpee, T. G. Slanger, D. L. Huestis, and P. C. Cosby, *Astrophys. J.* **606**, 605 (2004).

[30] T. M. Donahue, T. Parkinson, E. C. Zipf, J. P. Doering, W. G. Fastie, and R. E. Miller, *Planet. Space Sci.* **16**, 737 (1968).

[31] V. J. Abreu, S. C. Solomon, W. E. Sharp, and P. B. Hays, *J. Geophys. Res.* **88**, 4140 (1983).

[32] D. R. Bates, *Space Sci.* **40**, 893 (1992).

[33] B. Walker, M. Saeed, T. Breeden, B. Yang, and L. F. DiMauro, *Phys. Rev. A* **44**, 4493 (1991).

[34] B. L. G. Bakker, D. H. Parker, P. C. Samartzis, and T. N. Kitsopoulos, *J. Chem. Phys.* **112**, 5654 (2000).

[35] M. V. Exter, C. Fattinger, and D. Grischkowsky, *Opt. Lett.* **14**, 1128 (1989).

[36] R. A. Cheville and D. Grischkowsky, *Opt. Lett.* **20**, 1646 (1995).

[37] S. P. Jamison, J. Shen, D. R. Jones, R. C. Issac, B. Ersfeld, D. Clark, and D. A. Jaroszynsky, *J. Appl. Phys.* **93**, 4334 (2003).

[38] T. Löffler, F. Jacob, and H. G. Roskos, *Appl. Phys. Lett.* **77**, 453 (2000).

[39] D. J. Cook and R. M. Hochstrasser, *Opt. Lett.* **25**, 1210 (2000).

[40] M. Kress, T. Löffler, S. Eden, M. Thomson, and H. G. Roskos, *Opt. Lett.* **29**, 1120 (2004).

[41] F. Kadlec, C. Kadlec, P. Kužel, P. Slavíček, and P. Jungwirth, *J. Chem. Phys.* **120**, 912 (2004).

[42] C. A. Schmuttenmaer, *Chem. Rev.* **104**, 1759 (2004).

[43] H. Němec, F. Kadlec, S. Surendran, P. Kužel, and P. Jungwirth, *J. Chem. Phys.* **122**, 104503 (2005).

[44] H. Němec, F. Kadlec, C. Kadlec, P. Kužel, and P. Jungwirth, *J. Chem. Phys.* **122**, 104504 (2005).

[45] L. V. Keldysh, *Sov. Phys. – JETP* **20**, 1307 (1965).

[46] J. H. Posthumus, *Rep. Prog. Phys.* **67**, 623 (2004).

[47] G. Herzberg, ed., *Molecular Spectra and Molecular Structure*, Van Nostrand Rheinhold, New York (1950).

[48] S. Augst, D. D. Meyerhofer, D. Strickland, and S. L. Chin, *J. Opt. Soc. Am. B* **8**, 858 (1991).

[49] C. Ellert and P. B. Corkum, *Phys. Rev. A* **59**, R3170 (1999).

[50] M. J. Dewitt and R. J. Levis, *Phys. Rev. Lett.* **81**, 5101 (1998).

[51] I. V. Litvinyuk, K. F. Lee, P. W. Dooley, D. M. Rayner, D. M. Villeneuve, and P. B. Corkum, *Phys. Rev. Lett.* **90**, 233003 (2003).

[52] N. W. Ashcroft and N. D. Mermin, *Solid State Physics*, Holt, Rinehart and Winston, New York (1976).

[53] W. R. Smythe, *Static and Dynamic Electricity*, McGraw-Hill, New York (1968).

[54] F. F. Chen, *Introduction to plasma physics and controlled fusion. I. Plasma physics*, vol. 1, Plenum Press, New York (1984).

[55] K. P. Subramanian and V. Kumar, *J. Phys. B.: At. Mol. Opt. Phys.* **23**, 745 (1990).

[56] J. W. Fleming and R. P. Wayne, *Chem. Phys. Lett.* **32**, 135 (1975).

[57] S. Willitsch, F. Innocenti, J. M. Dyke, and F. Merkt, *J. Chem. Phys.* **122**, 024311 (2005).

List of figures:

Fig. 1: Experimental scheme. The pump beam branch contains a specific arrangement for a careful control of the pump beam attenuation and polarization and a second harmonic stage (see Appendix for further details). Inset: detail of the geometry of the aperture and beams and of the interaction volume.

Fig. 2: Potential curves of O_2 and O_2^+ with the most probable multiphoton excitation and ionization process at 405 nm denoted by arrows. The right-hand scale is normalized by the energy of 405 nm photons, i.e., it indicates the number of blue photons needed for a particular transition. Full arrow indicates the first resonant step, the dashed arrow indicates the second step involving the photoionization of the oxygen molecule.

Fig. 3: Schematic picture of the influence of the laser electric field on the Coulomb potential due to the positively charged core felt by the electron in the static approximation. The maximum available values of the electric field for both experimental wavelengths were assumed in the plot.

Fig. 4: Compilation of results showing the transient THz signal and free electron density versus pump intensity (linear polarization). Stars and crosses: both vertical scales are relevant; filled symbols: only left-hand scale is relevant, open symbols: only right-hand scale is relevant (as shown by the arrows). Inset: measured ratio between the transient THz signal for circularly and linearly polarized pump.

Fig. 5: Pump–probe scans: maximum field amplitude of the transient signal normalized by the maximum field amplitude of the reference waveform versus pump–probe delay.

Fig. 6: Transient field transmittance $\Delta t(\omega)$ at low pump intensity and the best fit using Drude model; pump wavelength: 405 nm; pump intensity: 3.2 TW/cm^2; pump–probe delay: $\tau_p = 10$

ps. Inset: corresponding equilibrium $E(\tau)$ and transient $\Delta E(\tau, \tau_p)$ waveforms.

Fig. 7: Dielectric spectra of electronic plasma in photo-ionized oxygen calculated from transient waveforms using Eq. (3) and the fits by the Drude-Lorentz model (10) for several pump pulse intensities. Optical pump at 405 nm, linearly polarized, $\tau_p = 10$ ps. Inset: momentum relaxation time τ_s extracted from the fits.

Fig. 8: Transient dielectric spectra obtained for $I = 12\,\mathrm{TW/cm^2}$ and two different pump–probe delays $\tau_p = 10, 60\,\mathrm{ps}$ and their fits using the Drude-Lorentz model (10) superposed with an underdamped harmonic oscillator at 39 $\mathrm{cm^{-1}}$ ($\tau_p = 10\,\mathrm{ps}$) and at 38 $\mathrm{cm^{-1}}$ ($\tau_p = 60\,\mathrm{ps}$). See the text for details. Inset: Imaginary part of the permittivity for several pump fluences (10.5–13.2 $\mathrm{TW/cm^2}$) at $\tau_p = 10\,\mathrm{ps}$.

Fig. 9: Transient field transmittance spectra $\Delta t(\omega)$ at $I = 12\,\mathrm{TW/cm^2}$ for the pump wavelength of 405 nm and for three significantly different pump–probe delays τ_p.

Fig. 10: Transformation of the pump beam in view of the intensity scaling for the two polarizations used. Pumping with (a) 405 nm, linear or circular polarizations; (b) 810 nm, linear polarization; (c) 810 nm, linear or circular polarizations. $\lambda/2$: half-wave plate, SHG: second harmonic generation, RP tunable retardation plate, BP: Brewster plate, GF: thin gray filter, FM: flipping mirror, PM: power meter.

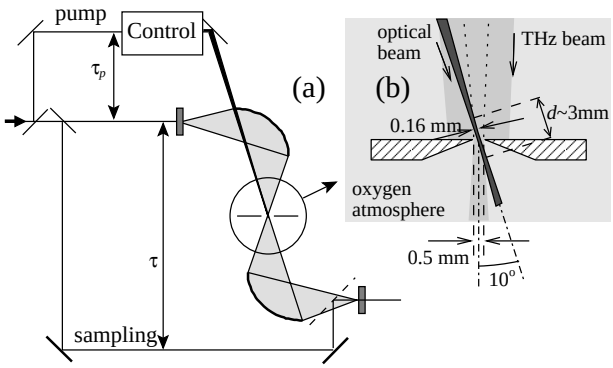

Figure 1: Z. Mics et al., J. Chem. Phys.

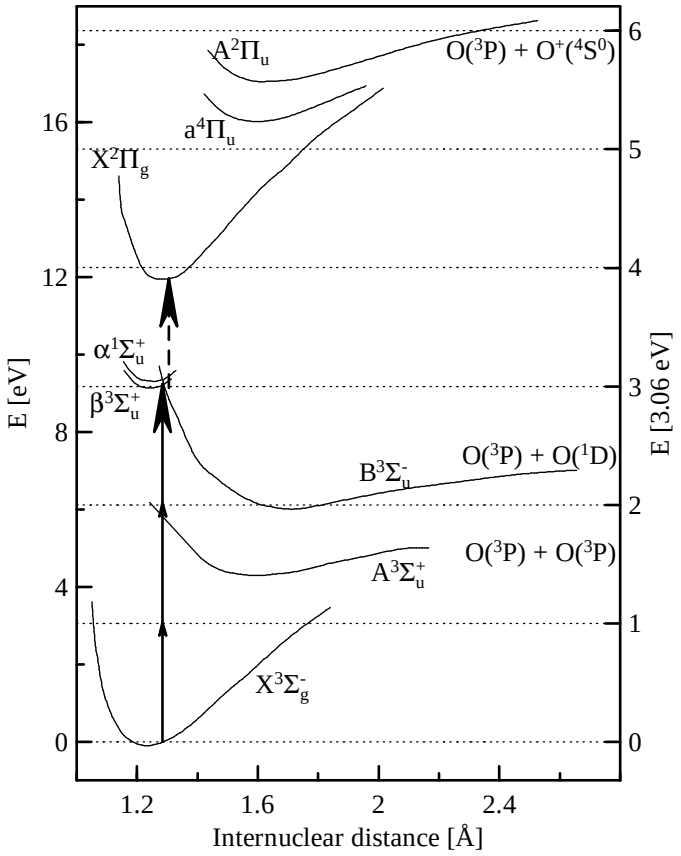

Figure 2: Z. Mics et al., J. Chem. Phys.

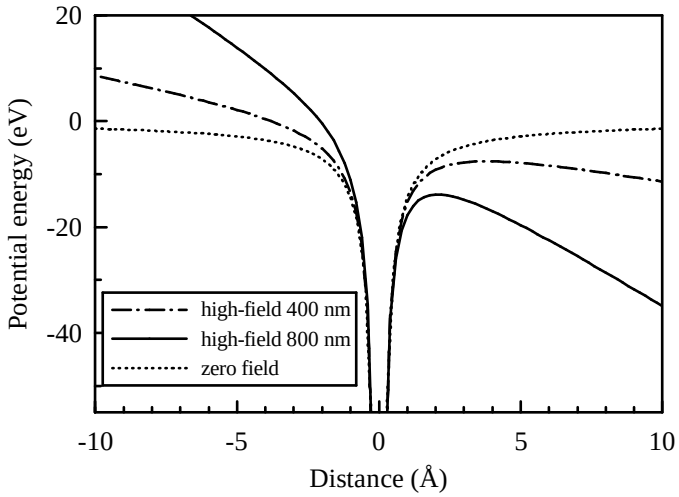

Figure 3: Z. Mics et al., J. Chem. Phys.

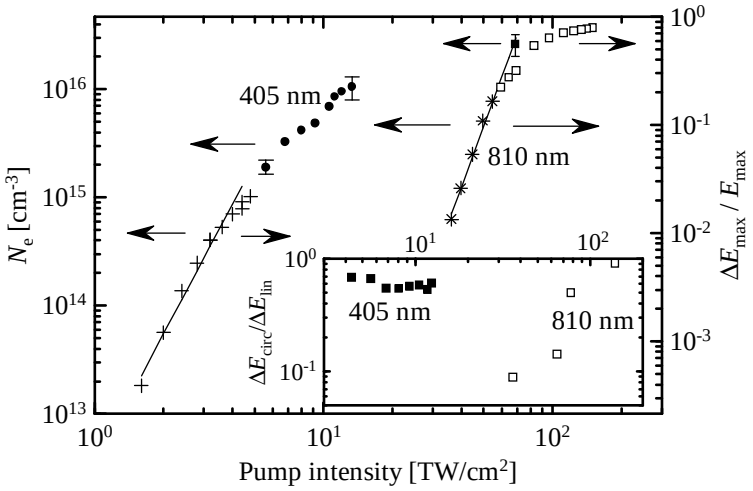

Figure 4: Z. Mics et al., J. Chem. Phys.

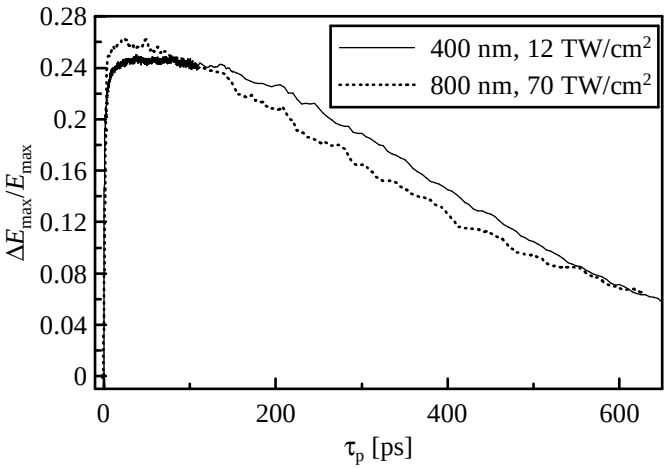

Figure 5: Z. Mics et al., J. Chem. Phys.

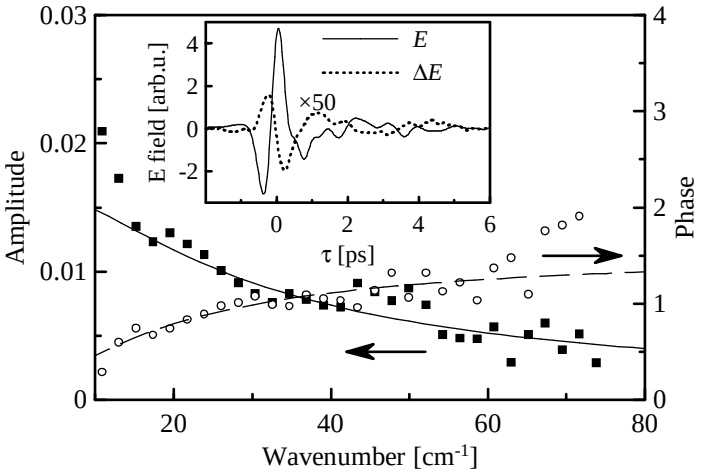

Figure 6: Z. Mics et al., J. Chem. Phys.

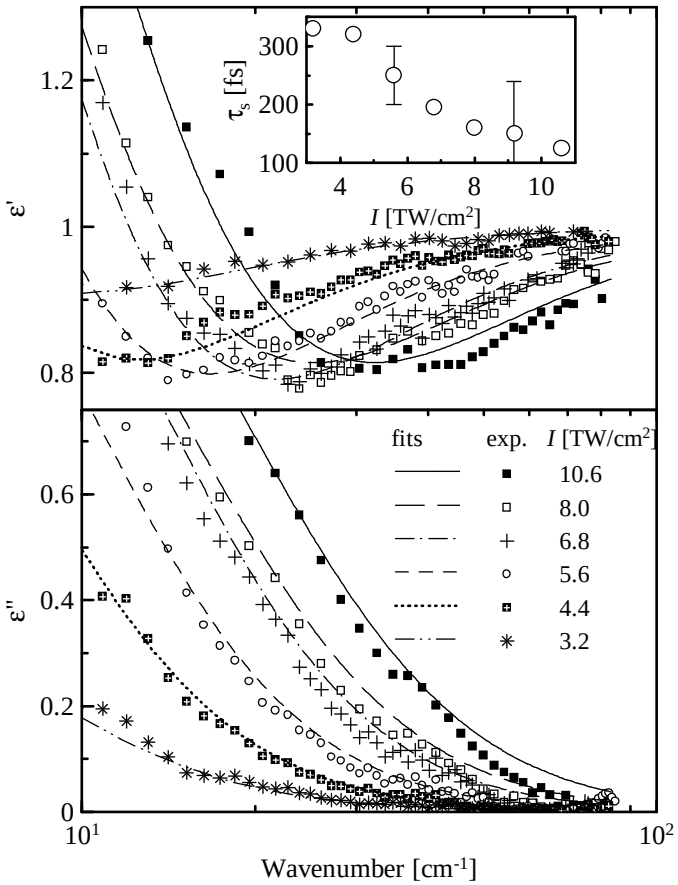

Figure 7: Z. Mics et al., J. Chem. Phys.

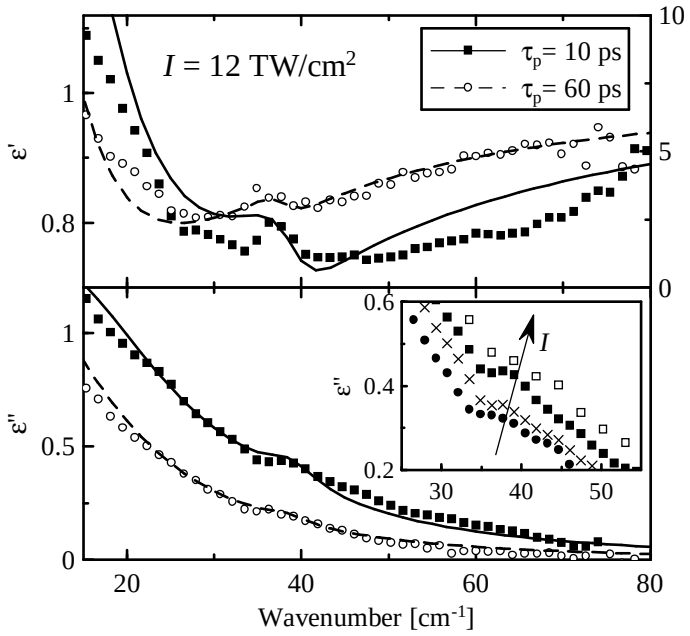

Figure 8: Z. Mics et al., J. Chem. Phys.

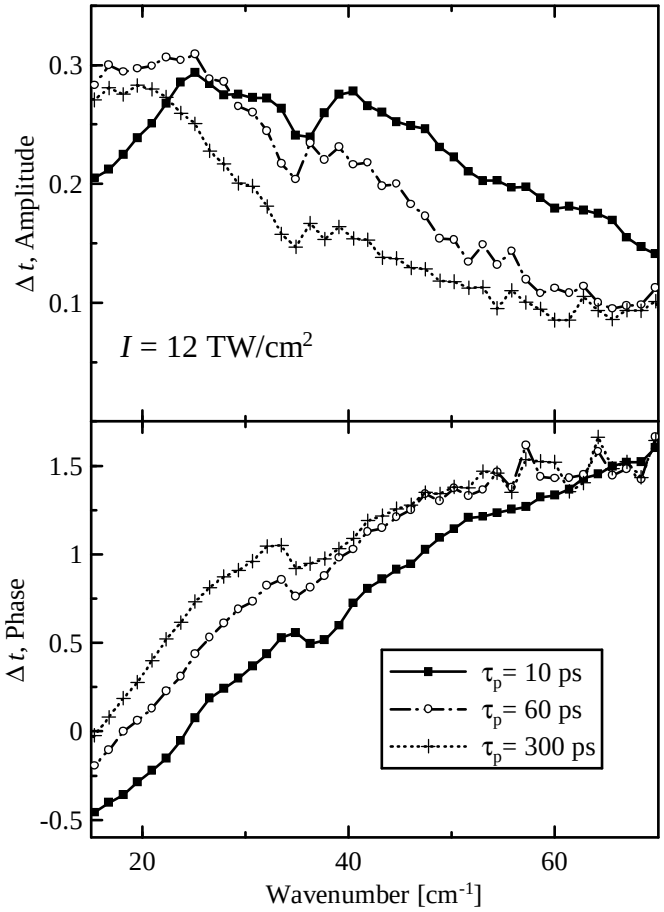

Figure 9: Z. Mics et al., J. Chem. Phys.

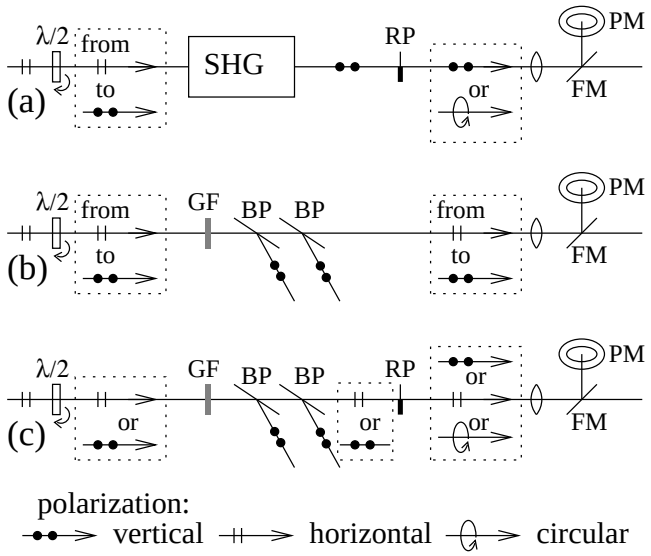

Figure 10: Z. Mics et al., J. Chem. Phys.